

Electron-phonon coupling and superconductivity in $\text{LiB}_{1+x}\text{C}_{1-x}$

QI-ZHI LI¹, XUN-WANG YAN², MIAO GAO^{1 (a)} and JUN WANG^{1 (b)}

¹ Department of Microelectronics Science and Engineering, Faculty of Science, Ningbo University - Zhejiang 315211, China

² College of Physics and Engineering, Qufu Normal University - Shandong 273165, China

PACS 74.70.Dd – Ternary, quaternary, and multinary compounds

PACS 74.20.Pq – Electronic structure calculations

PACS 63.20.kd – Phonon-electron interactions

Abstract – By means of the first-principles density-functional theory calculation and Wannier interpolation, electron-phonon coupling and superconductivity are systematically explored for boron-doped LiBC (i.e. $\text{LiB}_{1+x}\text{C}_{1-x}$), with x between 0.1 and 0.9. Hole doping introduced by boron atoms is treated through virtual-crystal approximation. For the investigated doping concentrations, our calculations show the optimal doping concentration corresponds to 0.8. By solving the anisotropic Eliashberg equations, we find that $\text{LiB}_{1.8}\text{C}_{0.2}$ is a two-gap superconductor, whose superconducting transition temperature, T_c , may exceed the experimentally observed value of MgB_2 . Similar to MgB_2 , the two-dimensional bond-stretching E_{2g} phonon modes along Γ - A line have the largest contribution to electron-phonon coupling. More importantly, we find that the first two acoustic phonon modes B_1 and A_1 around the midpoint of K - Γ line play a vital role for the rise of T_c in $\text{LiB}_{1.8}\text{C}_{0.2}$. The origin of strong couplings in B_1 and A_1 modes can be attributed to enhanced electron-phonon coupling matrix elements and softened phonons. It is revealed that all these phonon modes couple strongly with σ -bonding electronic states.

Introduction. – The discovery of 39 K superconductivity in MgB_2 [1] has aroused great interest in searching for new high-temperature superconductors whose pairing glue is electron-phonon coupling (EPC). Many compounds with similar atomic and/or electronic structures to MgB_2 have been extensively investigated, such as $M\text{B}_2$ ($M = \text{Be}$ [2–4], Na [5], Ca [3–7], Sc [3, 5], Cu [8], Sr [4, 5], Y [3, 5], Zr [5, 9], Ag [10], Ta [5, 11], Os [12], and Au [10]), CaBeSi [2], LiBC [13], and MgB_2C_2 [4]. Among these compounds, the most fascinating one is Li deficient Li_xBC , whose T_c is predicted to be above 100 K for x equal to 0.5.

In MgB_2 , the underlying physics for high- T_c superconductivity is the strong EPC between metallic covalent σ -bonding states and high-frequency E_{2g} phonons associated with bond-stretching movements of boron atoms [14–18]. For semiconducting LiBC, the valence band maximum (VBM) locates at the Γ - A line, corresponding to the σ -bonding states between boron and carbon atoms. Rosner and coworkers suggested that the σ -bonding states can be rigidly lifted up to the Fermi level by removing some Li atoms [13], forming Li_xBC . Thus the electronic struc-

ture of Li_xBC is reminiscent of that in MgB_2 . And the high- T_c superconductivity in Li_xBC seems natural. But evidence for superconductivity in Li_xBC is not available [19–21]. As a response to Li deficiency, the boron-carbon layer has drastic lattice distortions, which diminish the hope to metallize the boron-carbon σ -bonding states [22].

Considering the importance of Li atom in holding the crystal structure, replacing a certain amount of carbon atoms by boron atoms is regarded as a feasible way to realize hole doping in LiBC. Miao *et al.* used virtual-crystal approximation (VCA) to study the EPC of $\text{LiB}_{1.1}\text{C}_{0.9}$, and suggested the superconducting T_c is about 36 K [23]. We proposed a new compound $\text{Li}_3\text{B}_4\text{C}_2$ (i.e. $\text{LiB}_{1.33}\text{C}_{0.67}$), whose T_c is about 53.8 K, based on Wannier interpolation technique [24]. Another material $\text{Li}_4\text{B}_5\text{C}_3$ ($\text{LiB}_{1.25}\text{C}_{0.75}$), which is obtained through the substitution a BC_3 layer for one honeycomb B-C layer in LiBC, is calculated to be superconducting under 16.8 K [25]. Although the superconductivity in LiBC under several hole doping concentrations has been explored, it is interesting to know how high the T_c can reach and at which doping concentration the maximal T_c can be obtained in $\text{LiB}_{1+x}\text{C}_{1-x}$ compounds.

In this work, we employ first-principles calculation and

^(a)E-mail: gaomiao@nbu.edu.cn

^(b)E-mail: wangjun2@nbu.edu.cn

Wannier interpolation technique to investigate the EPC and superconductivity in $\text{LiB}_{1+x}\text{C}_{1-x}$, with x varying from 0.1 to 0.9 to determine the optimal doping concentration. Our calculation shows that the highest T_c can be achieved in $\text{LiB}_{1.8}\text{C}_{0.2}$. By solving the anisotropic Eliashberg equations, it is found that $\text{LiB}_{1.8}\text{C}_{0.2}$ is a two-gap superconductor, whose T_c may exceed the one of MgB_2 by a few Kelvin. At low doping, two-dimensional bond-stretching E_{2g} phonon modes at Γ point possess the largest contribution to EPC. Further increasing the hole doping concentration, B_1 and A_1 phonon modes at about $\frac{K\Gamma}{2}$ contribute enormously to the EPC, due to enhanced EPC matrix element and phonon softening.

Methods. – In our calculations the plane wave basis method is used [26]. We adopt the local density approximation (LDA) of Perdew-Zunger as the exchange-correlation functions. The norm-conserving pseudopotentials [27] are employed to model the electron-ion interactions. Since boron and carbon are neighboring in the periodic table, the hole doping introduced by boron is dealt with the VCA. Hereafter the virtual atom is labeled as X, whose atomic mass is taken as the geometric mean value for each doping level. The kinetic energy cut-off and the charge density cut-off of the plane wave basis are chosen to be 80 Ry and 320 Ry, respectively. The charge density is calculated on a $18 \times 18 \times 12$ \mathbf{k} -point grid and a Methfessel-Paxton smearing [28] with width of 0.02 Ry. For each doping concentration, the lattice constants and atomic positions are fully relaxed by minimizing the total energy [see Table I for details]. The phonons and the phonon perturbation potentials [29] are calculated on a Γ -centered $6 \times 6 \times 4$ mesh, within the framework of density-functional perturbation theory [30].

Maximally localized Wannier functions (MLWFs) [31, 32] are constructed on a $6 \times 6 \times 4$ grid of the Brillouin zone. Here we use eight Wannier functions to describe the band structure of $\text{LiB}_{1+x}\text{C}_{1-x}$ around the Fermi level. Two functions are p_z -like states associated with the X atoms, and six functions are σ -like states localized in the middle of B-X bonds. For example, the spatial spreads of the MLWFs that we generated in $\text{LiB}_{1.1}\text{C}_{0.9}$ are 2.79 \AA^2 for p_z -like states and 0.83 \AA^2 for σ -like states, respectively. Fine electron ($72 \times 72 \times 48$) and phonon ($24 \times 24 \times 16$) grids are used to interpolate the electron-phonon coupling (EPC) quantities with Wannier90 [33,34] and EPW codes [35,36]. Dirac δ -functions for electrons and phonons are replaced by smearing functions with widths of 125 meV and 0.2 meV, respectively. The EPC constant λ can be determined through summation over the Brillouin zone or integration of the Eliashberg spectral function $\alpha^2 F(\omega)$ in frequency space as [37,38],

$$\lambda = \frac{1}{N_q} \sum_{\mathbf{q}\nu} \lambda_{\mathbf{q}\nu} = 2 \int \frac{\alpha^2 F(\omega)}{\omega} d\omega. \quad (1)$$

The EPC constant $\lambda_{\mathbf{q}\nu}$ for mode ν at wavevector \mathbf{q} is

defined by [37,38],

$$\lambda_{\mathbf{q}\nu} = \frac{2}{\hbar N(0) N_k} \sum_{ij\mathbf{k}} \frac{1}{\omega_{\mathbf{q}\nu}} |g_{\mathbf{k},\mathbf{q}\nu}^{ij}|^2 \delta(\epsilon_{\mathbf{q}}^i) \delta(\epsilon_{\mathbf{k}+\mathbf{q}}^j). \quad (2)$$

Here N_q/N_k is the total number of \mathbf{q}/\mathbf{k} points in the fine Brillouin-zone mesh. $N(0)$ is the electronic density of states (DOS) at the Fermi energy. (i, j) and ν denote indices of energy bands and phonon modes, respectively. $\omega_{\mathbf{q}\nu}$ stands for the phonon frequency of the ν -th phonon mode with wavevector \mathbf{q} . $g_{\mathbf{k},\mathbf{q}\nu}^{ij}$ is the EPC matrix element. $\epsilon_{\mathbf{q}}^i$ and $\epsilon_{\mathbf{k}+\mathbf{q}}^j$ are eigenvalues of Kohn-Sham states with respect to the Fermi energy at given bands and momentums. The Eliashberg spectral function can be expressed as [37,38],

$$\alpha^2 F(\omega) = \frac{1}{2} \sum_{\mathbf{q}\nu} \delta(\omega - \omega_{\mathbf{q}\nu}) \lambda_{\mathbf{q}\nu} \omega_{\mathbf{q}\nu}. \quad (3)$$

Finally, the superconducting transition temperature (T_c) is determined by utilizing the McMillian-Allen-Dynes formula [38],

$$T_c = \frac{\omega_{\log}}{1.2} \exp \left[\frac{-1.04(1 + \lambda)}{\lambda(1 - 0.62\mu^*) - \mu^*} \right]. \quad (4)$$

μ^* is the effective screened Coulomb repulsion constant, namely Coulomb pseudopotential. ω_{\log} is the logarithmic average frequency, which can be computed through $\exp \left[\frac{2}{\lambda} \int \frac{d\omega}{\omega} \alpha^2 F(\omega) \log \omega \right]$.

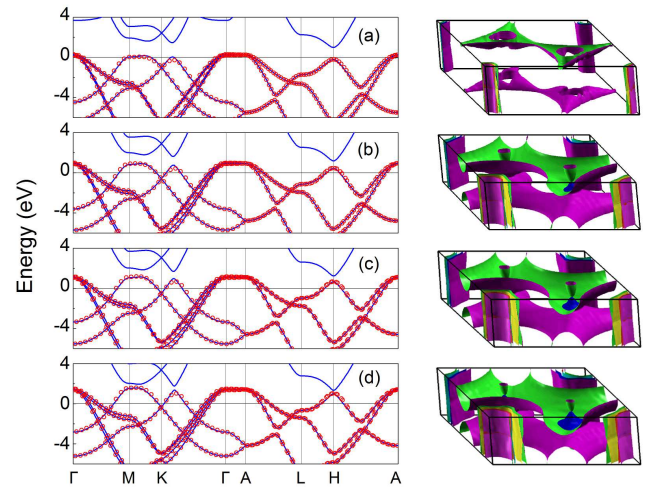


Fig. 1: (Color on-line) The band structures and Fermi surfaces of $\text{LiB}_{1+x}\text{C}_{1-x}$, with x being 0.1 (a), 0.5 (b), 0.6 (c), and 0.8 (d), respectively. The blue lines are calculated by the first principles, the red circles are obtained through MLWFs interpolation. The Fermi energy is set to zero.

Result and Analysis. – Figure 1 contains the band structures of $\text{LiB}_{1+x}\text{C}_{1-x}$. As we see, $\text{LiB}_{1.1}\text{C}_{0.9}$ already becomes a metal. Namely, the σ -bonding states at the

VBM have been successfully metallized. Thus the hole cylinders around Γ -A line are from σ -bonding bands [right panel of Fig. 1(a)]. Increasing hole doping concentration, the occupied energy bands almost move upward rigidly and the volumes enclosed by Fermi surfaces expand. While the location of empty energy bands is not affected by doping. As a consequence, the energy gap is gradually reduced, and close to zero for $\text{LiB}_{1.8}\text{C}_{0.2}$. The band structures obtained through interpolation of MLWFs are in excellent agreement with the ones calculated from first principles. It is noted that the empty energy bands are not included in the Wannier interpolation and subsequent EPC calculation. At H point, the value of conduction band minimum (CBM) is at least 1.0 eV. Physically, the electronic states that involved in EPC process are restricted to the Fermi level. Thus the exclusion of empty energy bands does not affect the accuracy of our EPC results.

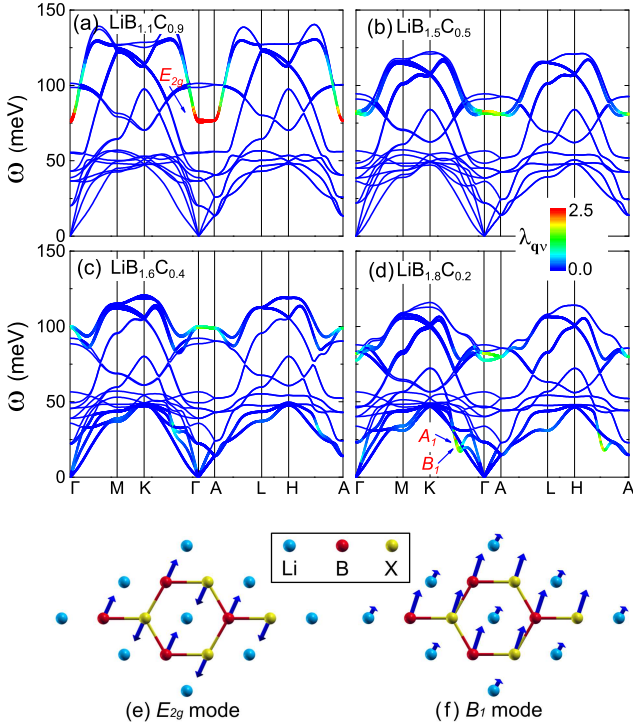


Fig. 2: (Color on-line) The phonon spectra of $\text{LiB}_{1.1}\text{C}_{0.9}$ (a), $\text{LiB}_{1.5}\text{C}_{0.5}$ (b), $\text{LiB}_{1.6}\text{C}_{0.4}$ (c), and $\text{LiB}_{1.8}\text{C}_{0.2}$ (d). The wavevector \mathbf{q} and mode index ν resolved EPC constant $\lambda_{\mathbf{q}\nu}$ is color mapped. (e) and (f) are the top views of real-space vibrational patterns for E_{2g} and B_1 phonon modes, respectively. The blue arrows and their lengths represent the directions and relative amplitudes of these vibration modes.

The phonon spectra weighted by $\lambda_{\mathbf{q}\nu}$ are shown in Fig. 2. For the selected doping interval, no imaginary phonon frequency is found, indicating the dynamical stability of $\text{LiB}_{1+x}\text{C}_{1-x}$. The strong EPC phonon modes, corresponding to the red lines along Γ -A, are E_{2g} modes, whose frequencies are listed in Table I. Although the frequency of E_{2g} mode fluctuates with the increase of doping

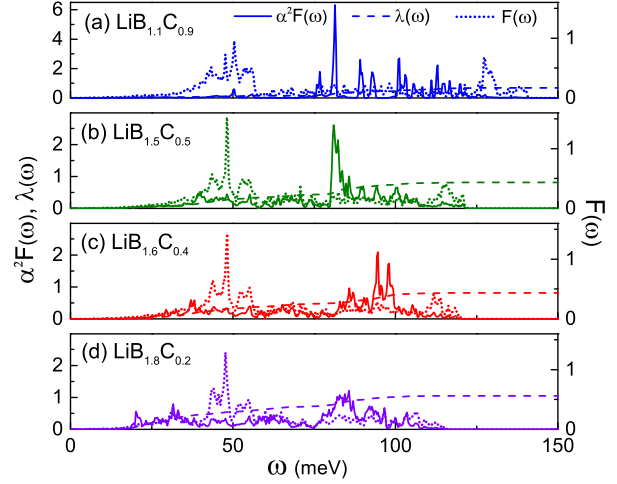


Fig. 3: (Color on-line) The calculated Eliashberg spectral function $\alpha^2F(\omega)$, $\lambda(\omega)$, and phonon density of states $F(\omega)$ of $\text{LiB}_{1+x}\text{C}_{1-x}$ for x equal to 0.1 (a), 0.5 (b), 0.6 (c), and 0.8 (d), respectively. $\lambda(\omega)$ is computed through $2 \int_0^\omega \frac{1}{\omega'} \alpha^2 F(\omega') d\omega'$.

concentration, an overall phonon softening is observed, especially, the first two acoustic phonon modes B_1 and A_1 at about $\frac{K\Gamma}{2}$ or $\frac{HA}{2}$ in $\text{LiB}_{1.8}\text{C}_{0.2}$ [see Fig. 2(d)]. The vibrational configurations of E_{2g} mode at Γ and B_1 mode at $\frac{K\Gamma}{2}$ are shown schematically in Fig. 2(e) and Fig. 2(f), respectively. The vibration of A_1 resembles that of B_1 , but with even smaller Li displacement. All these phonon modes mainly involve the two-dimensional movements of boron and virtual atoms.

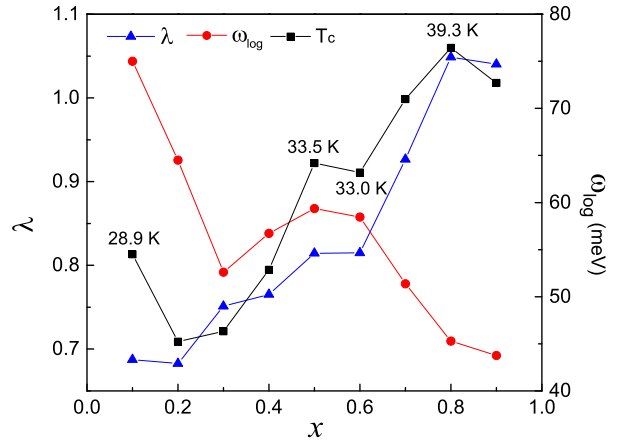


Fig. 4: (Color on-line) The calculated EPC constant λ , logarithmic average frequency ω_{\log} , and superconducting T_c for the investigated nine doping concentrations. The values of superconducting T_c are tagged next to the data points.

Compared with other three doping conditions, there is a very sharp peak for the Eliashberg spectral function $\alpha^2F(\omega)$ in $\text{LiB}_{1.1}\text{C}_{0.9}$ at about 80 meV associated with

the strongly coupled E_{2g} phonon modes [Fig. 3(a)]. Nevertheless, the spectral weight from the low-frequency region is almost zero. The amplitude of $\alpha^2 F(\omega)$ is gradually reduced with rising doping concentration, but the low-frequency part of $\alpha^2 F(\omega)$ becomes stronger and stronger [Fig. 3(b)-Fig. 3(d)], consistent with the emergence of strong coupling B_1 and A_1 phonon modes in the phonon spectra [Fig. 2].

Table 1: The optimized lattice constants, $N(0)$ (states/eV/atom/spin), frequency of E_{2g} (meV), λ , ω_{\log} (meV) and T_c (K) for different doping concentrations.

x	a (Å), c/a	$N(0)$	$\omega_{E_{2g}}$	λ	ω_{\log}	T_c
0.1	2.750, 2.602	0.07	76.9	0.69	75.0	28.9
0.2	2.767, 2.587	0.11	86.2	0.68	64.5	24.5
0.3	2.786, 2.567	0.13	87.5	0.75	52.6	25.0
0.4	2.806, 2.547	0.13	80.5	0.77	56.7	28.1
0.5	2.825, 2.530	0.11	82.8	0.81	59.4	33.5
0.6	2.846, 2.507	0.11	99.3	0.81	58.5	33.0
0.7	2.871, 2.473	0.11	92.9	0.93	51.4	36.7
0.8	2.895, 2.446	0.11	82.1	1.05	45.3	39.3
0.9	2.919, 2.423	0.11	84.7	1.04	43.8	37.5

The calculated EPC constant λ , logarithmic average frequency ω_{\log} , and T_c are presented in Fig. 4. For clarity, these quantities are also summarized in Table I. As we see, λ and T_c roughly display monotonous increasing versus the doping concentration. $\text{LiB}_{1.8}\text{C}_{0.2}$ possesses the maximal superconducting T_c of 39.3 K, slightly higher than that in MgB_2 . In the determination of T_c for $\text{LiB}_{1+x}\text{C}_{1-x}$, the Coulomb pseudopotential μ^* is set to 0.1. As pointed out in Ref. [39], an enhanced $N(0)$ can lead to an enhanced Coulomb pseudopotential. For most doping concentrations, the $N(0)$ of $\text{LiB}_{1+x}\text{C}_{1-x}$ is around 0.11 states/eV/atom/spin [see Table I]. Thus the usage of a single μ^* , i.e. 0.1, for all the doping concentrations is reasonable. Interestingly, $N(0)$ is also equal to 0.11 states/eV/atom/spin in MgB_2 from our Wannier interpolation.

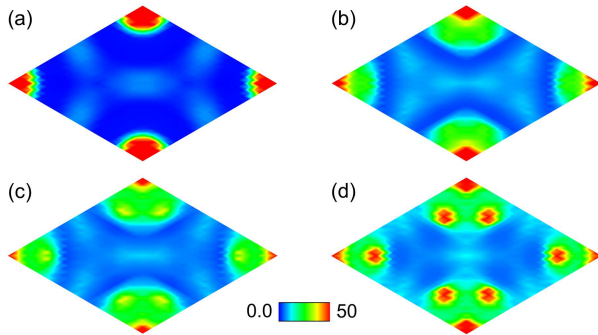


Fig. 5: (Color on-line) Top views of $\lambda(\mathbf{q}_{2D})$ in the reduced 2D Brillouin zone for $\text{LiB}_{1+x}\text{C}_{1-x}$ with x being 0.1 (a), 0.5 (b), 0.6 (c), and 0.8 (d), respectively.

Since $\text{LiB}_{1.1}\text{C}_{0.9}$ has the largest $\lambda_{\mathbf{q}\nu}$ from E_{2g} modes among these four doping situations along the Γ - A line [Fig. 2(a)], it is surprising that the smallest λ is found in $\text{LiB}_{1.1}\text{C}_{0.9}$. This suggests that there exist sizeable $\lambda_{\mathbf{q}\nu}$ s, which are not clearly reflected along the high-symmetry line in other three doping levels. To unambiguously confirm above assumption, we plot $\lambda(\mathbf{q}_{2D})$, defined by $\sum_{\mathbf{q}_2\nu} \lambda_{\mathbf{q}\nu}$, in reduced two-dimensional (2D) Brillouin zone [Fig. 5]. Even though there is a big red spot around Γ point in $\text{LiB}_{1.1}\text{C}_{0.9}$, the $\lambda(\mathbf{q}_{2D})$ is close to zero in other area of the Brillouin zone [Fig. 5(a)]. In sharp contrast, considerable $\lambda(\mathbf{q}_{2D})$ emerges beside Γ point, especially for $\text{LiB}_{1.8}\text{C}_{0.2}$ [Fig. 5(d)], in which six bright spots obviously appear at $\frac{K\Gamma}{2}$ and its equivalent points. These spots exactly come from the B_1 and A_1 phonon modes [Fig. 2(d)], which thus have vital importance for the enhancement of λ and T_c upon the increasing of hole doping.

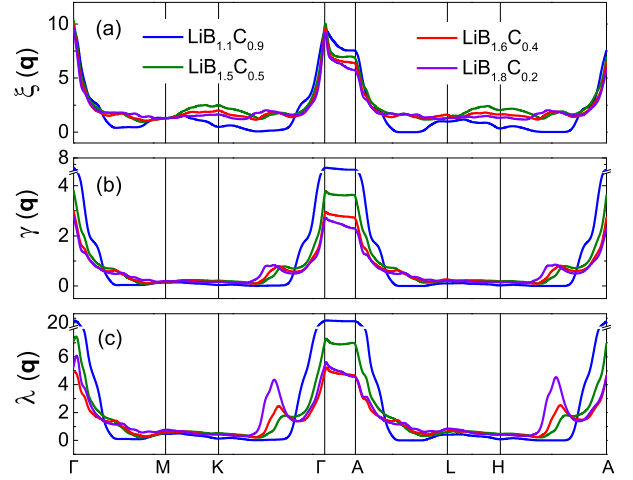


Fig. 6: (Color on-line) $\xi(\mathbf{q})$, $\gamma(\mathbf{q})$, and $\lambda(\mathbf{q})$ for $\text{LiB}_{1+x}\text{C}_{1-x}$.

In order to identify the origin of the strong EPC B_1 and A_1 phonon modes, we calculate $\xi(\mathbf{q})$ and $\gamma(\mathbf{q})$, which read

$$\xi(\mathbf{q}) = \frac{1}{N_k} \sum_{ij\mathbf{k}} \delta(\epsilon_{\mathbf{k}}^i) \delta(\epsilon_{\mathbf{k}+\mathbf{q}}^j) \quad (5)$$

and

$$\gamma(\mathbf{q}) = \frac{1}{N_k} \sum_{ij\nu\mathbf{k}} |g_{\mathbf{k},\mathbf{q}\nu}^{ij}|^2 \delta(\epsilon_{\mathbf{k}}^i) \delta(\epsilon_{\mathbf{k}+\mathbf{q}}^j), \quad (6)$$

respectively. $\xi(\mathbf{q})$ is the Fermi surface nesting function. $\gamma(\mathbf{q})$ is the summation of EPC matrix element $|g_{\mathbf{k},\mathbf{q}\nu}^{ij}|$ around the Fermi level. $\xi(\mathbf{q})$ is almost the same with each other for the studied cases [Fig. 6(a)]. This indicates that the Fermi surface nesting function $\xi(\mathbf{q})$ is not a dominant factor for strong EPC in B_1 and A_1 modes. We find that there are humps in $\gamma(\mathbf{q})$ at the middle point of K - Γ or H - A for the later three concentrations [Fig. 6(b)], reflecting the aggrandizement of EPC matrix elements around the Fermi level. These humps are further amplified in $\lambda(\mathbf{q})$ by

phonon softening [Fig. 6(c) and Fig. 2(d)]. Thus, both enhanced EPC matrix element $|g_{\mathbf{k},\mathbf{q}\nu}^{ij}|$ and softened B_1 and A_1 phonon modes account for the occurrence of strong EPC.

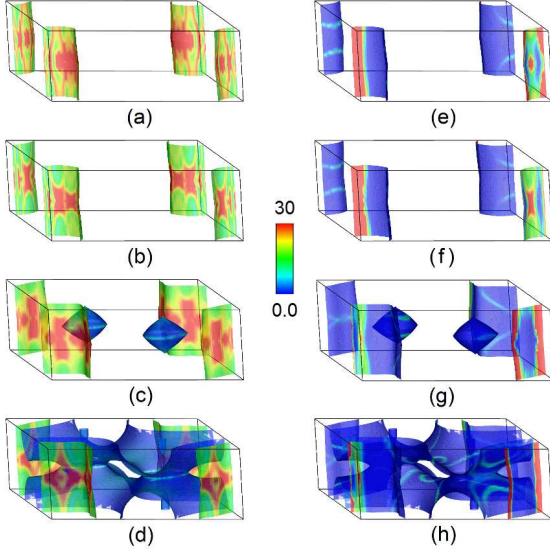


Fig. 7: The calculated $\lambda_{\mathbf{k}i}$ in $\text{LiB}_{1.8}\text{C}_{0.2}$ for \mathbf{q} being Γ (a-d) and $\frac{K\Gamma}{2}$ (e-h), respectively. There are four bands crossing the Fermi level in $\text{LiB}_{1.8}\text{C}_{0.2}$ [Fig. 1(d)]. The Fermi surfaces formed by the four bands are plotted separately with ascending band energy from (a)/(e) to (d)/(h).

Another important question should be addressed is which electrons strongly couple with E_{2g} mode at Γ and B_1/A_1 mode at $\frac{K\Gamma}{2}$. Here we introduce a new quantity $\lambda_{\mathbf{k}i}$, which represents the EPC constant at given momentum \mathbf{k} and band i .

$$\lambda_{\mathbf{k}i} = \frac{2}{\hbar N(0)} \sum_{j\nu} \frac{1}{\omega_{\mathbf{q}\nu}} |g_{\mathbf{k},\mathbf{q}\nu}^{ij}|^2 \delta(\epsilon_{\mathbf{k}}^i) \delta(\epsilon_{\mathbf{k}+\mathbf{q}}^j), \quad (7)$$

Here j is also the index of electronic energy band. By specifying the phonon wavevector \mathbf{q} , one can explicitly determine the electrons states that have large coupling with phonon modes at this wavevector. To be specific, we calculate $\lambda_{\mathbf{k}i}$ in $\text{LiB}_{1.8}\text{C}_{0.2}$ for \mathbf{q} being Γ and $\frac{K\Gamma}{2}$, respectively [Fig. 7]. It is found that the E_{2g} phonon mode mainly couples with the cylinder-like hole Fermi surfaces around Γ - A line [Fig. 7(a)-Fig. 7(d)]. This is also the case for B_1 and A_1 modes [Fig. 7(e)-Fig. 7(h)]. As we know, these cylindrical Fermi surfaces correspond to the B-X σ -bonding bands. So the high- T_c superconductivity in $\text{LiB}_{1+x}\text{C}_{1-x}$ originates from strong coupling between phonon modes (i.e. E_{2g} mode at Γ and B_1/A_1 mode at $\frac{K\Gamma}{2}$) and B-X σ -bonding bands.

With respect to the semi-empirical McMillian-Allen-Dynes formula, the superconducting T_c can also be determined by solving the anisotropic Eliashberg equations. Besides T_c , this method can provide more information

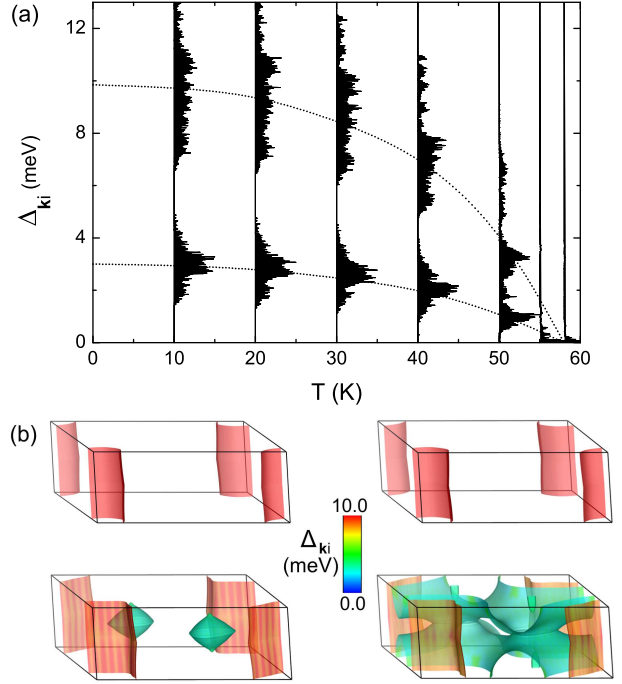


Fig. 8: Superconducting properties of $\text{LiB}_{1.8}\text{C}_{0.2}$ obtained by solving the anisotropic Eliashberg equations. (a) Calculated anisotropic superconducting gap $\Delta_{\mathbf{k}i}$ on the Fermi surface as a function of temperature. The histograms at each temperature indicate the number of states on the Fermi surface with that superconducting gap energy. The dotted lines are guides to the eye. (b) Distribution of superconducting energy gaps on the four Fermi surfaces at 10 K.

about the superconducting gap structure. For example, the two-gap structure in MgB_2 is clearly revealed by anisotropic Eliashberg calculations [40–43]. Bekaert *et al.*, further studied the novel superconducting gap resulted from the surface state in monolayer MgB_2 [44] or few-layer MgB_2 [45].

For the sake of making T_c in $\text{LiB}_{1+x}\text{C}_{1-x}$ more reasonable, we solve the anisotropic Eliashberg equations along the imaginary axis for $\text{LiB}_{1.8}\text{C}_{0.2}$. The superconducting gaps are determined from the approximate Padé continuation, and the Coulomb potential is chosen to be 0.16. The reason for using 0.16 is to directly compare our result with that of MgB_2 given in Ref. [36, 40]. We can identify two distinct sets of superconducting gaps for $\text{LiB}_{1.8}\text{C}_{0.2}$ [Fig. 8(a)], which are associated with the σ and the π sheets of the Fermi surface [Fig. 8(b)]. By taking the Fermi-surface averages, these gaps are $\Delta_\pi=2.8$ meV and $\Delta_\sigma=9.5$ meV at 10 K, which are about 12% and 5.6% larger than that in MgB_2 [36], respectively. The two superconducting gaps vanish at 58 K, which is 7 K higher than the value of MgB_2 obtained by Ref. [36] with the same calculation method. It is noteworthy that anharmonic effect of phonons should be taken into consideration to reconcile

theoretically calculated T_c with experimentally observed one for MgB_2 [42, 43, 46]. But the investigation of anharmonic effect in $\text{LiB}_{1+x}\text{C}_{1-x}$ is not the purpose of this work. The hot zones of anisotropic electron-phonon coupling strength λ are mainly distributed on the σ Fermi sheets [Fig. 8(b)]. This further confirms the results presented in Fig. 7.

Discussion and Conclusion. – The sampling points contained in our fine \mathbf{k} -mesh for electrons and \mathbf{q} -mesh for phonons are 42 times more than that used in previous simulation of $\text{LiB}_{1.1}\text{C}_{0.9}$ [23]. Thus our T_c of $\text{LiB}_{1.1}\text{C}_{0.9}$ should be more reliable. It is noted that the superconducting T_c of $\text{Li}_3\text{B}_4\text{C}_2$ [24] or $\text{Li}_4\text{B}_5\text{C}_3$ [25] is different from the trend determined in our calculations. The reasons for this inconsistency are twofold. Firstly, the distribution of boron and carbon atoms in $\text{LiB}_{1+x}\text{C}_{1-x}$ is not included in the VCA. Different distributions will result in different electronic states, phonons, and T_c . Secondly, the crystal structures used by $\text{Li}_3\text{B}_4\text{C}_2$ and $\text{Li}_4\text{B}_5\text{C}_3$ may be not the ground-state structures at corresponding stoichiometry. Considering several intelligent crystal structure prediction methods have been developed, such as random sampling method [47], particle-swarm optimization [48], and evolutionary technique [49], the ground-state structure of $\text{LiB}_{1.8}\text{C}_{0.2}$ is called for to verify our prediction.

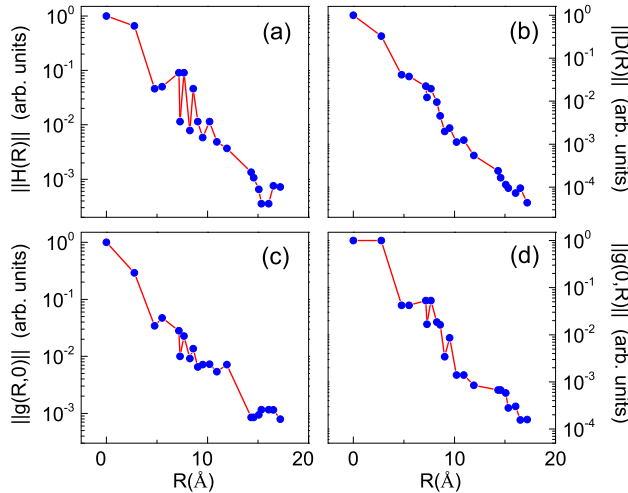


Fig. 9: (Color on-line) Spatial decays of the electronic Hamiltonian $\|H(R)\|$, the dynamical matrix $\|D(R)\|$, and the EPC matrix element $\|g(R,0)\|$ and $\|g(0,R)\|$ in the Wannier representation for $\text{LiB}_{1.1}\text{C}_{0.9}$. For the explicit definitions of above four quantities, please see Ref. [29].

In conclusion, we have extensively studied the EPC and phonon-mediated superconductivity for boron doped LiBC, utilizing the first-principles calculations and the state-of-the-art Wannier interpolation technique. At the VCA level, the maximal superconducting T_c for $\text{LiB}_{1+x}\text{C}_{1-x}$ may slightly surpass that of MgB_2 , with the optimal doping concentration x being 0.8. Beside the commonly known E_{2g} phonon mode in MgB_2 , we find that the

B_1 and A_1 phonon modes, which mainly involve the two-dimensional movements of boron and the boron-carbon virtual atoms, have strong coupling with the σ -bonding electronic states.

This research is supported by Zhejiang Provincial Natural Science Foundation of China under Grant No. LY17A040005, and National Natural Science Foundation of China (Grant Nos. 11474004, 11404383, 11474174, and 11674185). M.G. is also sponsored by K.C.Wong Magna Fund in Ningbo University.

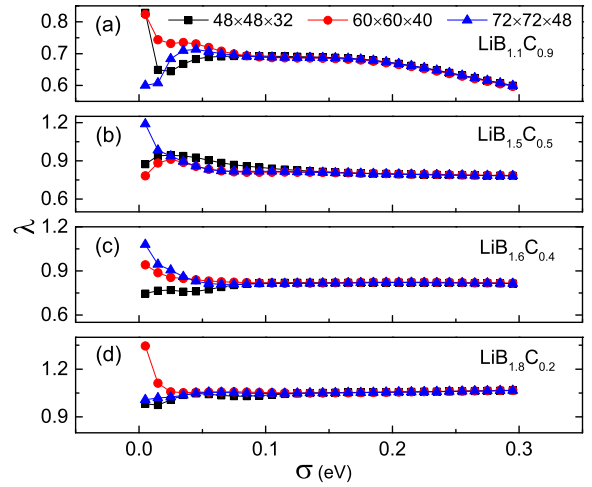


Fig. 10: (Color on-line) Convergence test of EPC constant λ versus electron smearing σ . The fine \mathbf{q} -mesh is $24 \times 24 \times 16$. (a) $\text{LiB}_{1.1}\text{C}_{0.9}$, (b) $\text{LiB}_{1.5}\text{C}_{0.5}$, (c) $\text{LiB}_{1.6}\text{C}_{0.4}$, (d) $\text{LiB}_{1.8}\text{C}_{0.2}$.

Appendix: Convergence test of EPC constant.

– The difficulty to obtain convergent EPC constant λ stems from the so-called double- δ -function approximation [Eq. (2)]. Millions of \mathbf{k} points are commonly needed to accurately describe the electron-phonon scattering in the vicinity of the Fermi surface. This is time demanding and hardly accomplished by regular first-principles calculations. However, the state-of-the-art Wannier interpolation technique can achieve this goal by generalized Fourier transformations, simultaneously keeping the accuracy of the first principles [29].

Since the reliability of Wannier interpolation strongly depends on the localizations of the electronic Hamiltonian, the dynamical matrix, and the EPC matrix element in the Wannier representation, thus we have carefully examined above quantities, which demonstrate excellent exponential decay [Fig. 9]. Three sets of fine \mathbf{k} -meshes (i.e. $48 \times 48 \times 32$, $60 \times 60 \times 40$, and $72 \times 72 \times 48$) are used to check at which smearing σ the λ is convergent [Fig. 10]. As σ approaching the zero limit, the curves of λ calculated by the two denser \mathbf{k} -meshes begin to bifurcate for σ being 125 meV [Fig. 10(c)]. Thus we regard the EPC properties gained

at 125 meV as the convergent ones, which have been presented in the main text. It is noted that the convergence of \mathbf{k} -dependent superconducting gap $\Delta_{\mathbf{k}i}$ is more challenging than for λ . As shown by Margine *et al.*, the energy distribution of σ gap is changed from 2.5 meV to 1.5 meV when increasing the fine \mathbf{q} -mesh from 20^3 to 40^3 , but the value of λ is not affected [40]. Here, careful examination for the convergence of $\Delta_{\mathbf{k}i}$ is not actualized, we adopt directly the convergent parameters for λ to calculate the superconducting gap [Fig. 8].

REFERENCES

- [1] NAGAMATSU J. *et al.*, *Nature (London)*, **410** (2001) 63.
- [2] SATTÀ G., PROFETA G., BERNARDINI F., CONTINENZA A. and MASSIDDA S., *Phys. Rev. B*, **64** (2001) 104507.
- [3] MEDVEDEVA N. I., IVANOVSKII A. L., MEDVEDEVA J. E. and FREEMAN A. J., *Phys. Rev. B*, **64** (2001) 020502(R).
- [4] RAVINDRAN P., VAJEESTON P., VIDYA R., KJEKSHUS A. and FJELLVÅG H., *Phys. Rev. B*, **64** (2001) 224509.
- [5] OGUCHI T., *J. Phys. Soc. Jpn.*, **71** (2002) 1495.
- [6] MEDVEDEVA N. I., MEDVEDEVA J. E., IVANOVSKII A. L., ZUBKOV V. G. and FREEMAN A. J., *JETP Lett.*, **73** (2001) 336.
- [7] CHOI H. J., LOUIE S. G. and COHEN M. L., *Phys. Rev. B*, **80** (2009) 064503.
- [8] MEHL M. J., PAPACONSTANTOPOULOS D. A. and SINGH D. J., *Phys. Rev. B*, **64** (2001) 140509(R).
- [9] GASPAREV V. A., SIDOROV N. S., ZVERKOVA I. I. and KULAKOV M. P., *JETP Lett.*, **73** (2001) 532.
- [10] KWON S. K., YOUN S. J., KIM K. S. and MIN B. I., arXiv:cond-mat/0106483.
- [11] ROSNER H., PICKETT W. E., DRECHSLER S.-L., HANDSTEIN A., BEHR G., FUCHS G., NENKOV K., MILLER K.-H. and ESCHRIG H., *Phys. Rev. B*, **64** (2001) 144516.
- [12] SINGH Y., NIAZI A., VANNETTE M. D., PROZOROV R. and JOHNSTON D. C., *Phys. Rev. B*, **76** (2007) 214510.
- [13] ROSNER H., KITAIGORODSKY A. and PICKETT W. E., *Phys. Rev. Lett.*, **88** (2002) 127001.
- [14] AN J. M. and PICKETT W. E., *Phys. Rev. Lett.*, **86** (2001) 4366.
- [15] KONG Y., DOLGOV O. V., JEPSEN O. and ANDERSEN O. K., *Phys. Rev. B*, **64** (2001) 020501(R).
- [16] YILDIRIM T. *et al.*, *Phys. Rev. Lett.*, **87** (2001) 037001.
- [17] CHOI H. J., ROUNDY D., SUN H., COHEN M. L. and LOUIE S. G., *Phys. Rev. B*, **66** (2002) 020513.
- [18] CHOI H. J., ROUNDY D., SUN H., COHEN M. L. and LOUIE S. G., *Nature*, **418** (2002) 758.
- [19] BHARATHI A. *et al.*, *Solid State Commun.*, **124** (2002) 423.
- [20] SOUPTELA D., HOSSAINB Z., BEHRA G., LÖSERA W. and GEIBEL C., *Solid State Commun.*, **125** (2003) 17.
- [21] FOGG A. M., CHALKER P. R., CLARIDGE J. B., DARLING G. R. and ROSSEINSKY M. J., *Phys. Rev. B*, **67** (2003) 245106.
- [22] FOGG A. M., MELDRUM J., DARLING G. R., CLARIDGE J. B. and ROSSEINSKY M. J., *J. Am. Chem. Soc.*, **128** (2006) 10043.
- [23] MIAO R. *et al.*, *J. Appl. Phys.*, **113** (2013) 133910.
- [24] GAO M., LU Z.-Y. and XIANG T., *Phys. Rev. B*, **91** (2015) 045132.
- [25] BAZHIROV T., SAKAI Y., SAITO S. and COHEN M. L., *Phys. Rev. B*, **89** (2014) 045136.
- [26] GIANNOZZI P. *et al.*, *J. Phys.: Condens. Matter*, **21** (2009) 395502.
- [27] TROULLIER N. and MARTINS J. L., *Phys. Rev. B*, **43** (1991) 1993.
- [28] METHFESSEL M. and PAXTON A. T., *Phys. Rev. B*, **40** (1989) 3616.
- [29] GIUSTINO F., COHEN M. L. and LOUIE S. G., *Phys. Rev. B*, **76** (2007) 165108.
- [30] BARONI S., GIRONCOLI S. D., CORSO A. D. and GIANNOZZI P., *Rev. Mod. Phys.*, **73** (2001) 515.
- [31] MARZARI N. and VANDERBILT D., *Phys. Rev. B*, **56** (1997) 12847.
- [32] SOUZA I., MARZARI N. and VANDERBILT D., *Phys. Rev. B*, **65** (2001) 035109.
- [33] MOSTOFI A. A., YATES J. R., LEE Y.-S., SOUZA I., VANDERBILT D. and MARZARI N., *Comput. Phys. Commun.*, **178** (2008) 685.
- [34] MOSTOFI A. A., YATES J. R., PIZZI G., LEE Y.-S., SOUZA I., VANDERBILT D. and MARZARI N., *Comput. Phys. Commun.*, **185** (2014) 2309.
- [35] NOFFSINGER J., GIUSTINO F., MALONE B. D., PARK C.-H., LOUIE S. G. and COHEN M. L., *Comput. Phys. Commun.*, **181** (2010) 2140.
- [36] PONCÉ S., MARGINE E. R., VERDI C. and GIUSTINO F., *Comput. Phys. Commun.*, **209** (2016) 116.
- [37] ALLEN P. B., *Phys. Rev. B*, **6** (1972) 2577.
- [38] ALLEN P. B. and DYNES R. C., *Phys. Rev. B*, **12** (1975) 905.
- [39] JIN Y.-G. and CHANG K. J., *Phys. Rev. B*, **57** (1998) 14684.
- [40] MARGINE E. R. and GIUSTINO F., *Phys. Rev. B*, **87** (2013) 024505.
- [41] APERIS A., MALDONADO P., and OPPENEER P. M., *Phys. Rev. B*, **92** (2015) 054516.
- [42] CHOI H. J., ROUNDY D., SUN H., COHEN M. L., and LOUIE S. G., *Phys. Rev. B*, **66** (2002) 020513(R).
- [43] CHOI H. J., ROUNDY D., SUN H., COHEN M. L., and LOUIE S. G., *Nature*, **418** (2002) 758.
- [44] BEKAERT J., APERIS A., PARTOENS B., OPPENEER P. M., and MILOŠEVIĆ M. V., *Phys. Rev. B*, **96** (2017) 094510.
- [45] BEKAERT J. *et al.*, *Sci. Rep.*, **7** (2017) 14458.
- [46] YILDIRIM T. *et al.*, *Phys. Rev. Lett.*, **87** (2001) 037001.
- [47] PICKARD C. J. and NEEDS R., *J. Phys.: Condens. Matter*, **23** (2011) 053201.
- [48] WANG Y., LV J., ZHU L. and MA Y., *Phys. Rev. B*, **82** (2010) 094116.
- [49] OGANOV A. R. and GLASS C. W., *J. Chem. Phys.*, **124** (2006) 244704.